Recovering Endocardial Walls from 3D TEE

Philippe Burlina[1,2], Ryan Mukherjee[1], Radford Juang[1], and Chad Sprouse[1]

[1] Johns Hopkins University Applied Physics Laboratory
philippe.burlina@jhuapl.edu
[2] Johns Hopkins University Department of Computer Science

Abstract. We describe a method for recovering the left intracardiac cavities from 3D Transesophageal Echocardiography (3D TEE). 3D TEE is an important modality for cardiac applications because of its ability to do fast and non-ionizing 3D imaging of the left heart complex. Segmentation based on 3D TEE can be used to characterize pathophysiologies of the valve and myocardium, and as input to patient-specific biomechanical models and preoperative planning tools. The segmentation employed here is based on a dynamic surface evolution. This is performed under a growth inhibition function that incorporates information from several sources including k-means clustering, 3D gradient magnitude, and a morphological structure tensor intended to locate the mitral valve leaflets. We report experiments using intraoperative 3D TEE data, showing good agreement between the segmented structures and ground truth.

1 Introduction

Segmentation of left heart endocardial wall structure has a number of applications in diagnostics, modeling, simulation and training, or as a primitive to other 3D ultrasound image analysis modules [1–3]. It is useful for performing preoperative planning, and for guiding minimally-invasive beating heart interventions, which are of interest as an alternative to procedures requiring cardiopulmonary bypass. 3D TEE is an important cardiac imaging modality to infer endocardial structure. It has a number of advantages compared to other 3D imaging modalities: it has a small form factor, is non-ionizing, has lower cost, it can be used pre- and intra-operatively, and it allows for interactive exploration and diagnostics. Another important advantage of 3D TEE for cardiac applications, is its speed, which is unmatched by other modalities. Sequences can be acquired at rates from 20 Hz up to over 60 Hz. This capability is essential when considering the very fast motion of some left heart anatomical components such as the mitral valve. Unfortunately 3D echocardiography has certain shortcomings which makes segmentation based on this modality a challenging endeavor. These include lower spatial resolution and imaging artifacts such as obscuration, speckle noise, and misalignments. Some 3D TEE platforms need to acquire and recombine subsections of the TEE data cube obtained over several heart cycles using a breath hold protocol to achieve both high spatial and temporal resolutions. When the patient exhibits arrhythmia the stitching of the TEE data cube subsections may lead to misalignment artifacts.

D.N. Metaxas and L. Axel (Eds.): FIMH 2011, LNCS 6666, pp. 284–293, 2011.

There are many approaches to the segmentation and recovery of cardiac structures. Recent surveys providing an overview of ultrasound segmentation methods include [4–6]. Among these methods, segmenting the structure of the left ventricle remains a primary focus. Techniques used for left ventricle segmentation include the following: (a) active models and model matching (active appearance models (AAMs), active shape models (ASMs), and their variants) [7–9]; (b) evolving curves and surfaces (e.g., active contour, level set, marching cube) [10–16]; (c) watershed [17]; (d) graph cuts [18]; (e) thresholding and morphology [19]; and (f) random forest classification [20].

Active models, such as AAMs and ASMs, most often require a user-generated model for training, which can take the form of a manually segmented point cloud. By finding an optimal set of parameter values for the user-generated model, it can be used to match image intensity values in a testing set. Mitchell et al. formulated a ventricle segmentation method that uses a combination of AAMs and ASMs to prevent the method's convergence towards local minima and automate the initialization process, which had previously been a major disadvantage to AAM-based methods [7]. However, that method was designed for 2D data with low amounts of noise (magnetic resonance imagery). We argue that the initialization method used might be challenged with more noisy ultrasound data and that rapid manual initialization might be more robust than automated methods when dealing with irregular and/or diseased hearts and atypical TEE viewpoints.

Evolving curves and surfaces simply requires an initial seed point or surface. Manual seed points can be rapidly entered by a physician to segment a variety of structures from atypical or unexpected views of the structures. The initial seeds are iteratively evolved (outward or inward) according to an energy function until some constraint or convergence criteria is met. Identifying a robust energy function that is also adequate for the TEE modality is an important task.

Less versatile and noise sensitive watershed algorithms treat the intensity values of images as valleys and peaks. Initial seed points are assigned labels, then valleys and peaks are "flooded" at the seed points. Pixels that are connected to the seed are assigned that seed's label.

Graph cuts algorithms treat each pixel/voxel as a node in a graph. Each node of the graph is connected to other nodes of the graph by some neighborhood scheme. Each node is also connected to a source and sink terminal node. The nodes are connected to other nodes by edges with assigned cost values. By performing a minimum cost cut on the graph, an optimal function can be solved that identifies whether a node belongs to the source or sink. A node that belongs to a source is considered part of the segmented structure. A node that belongs to the sink is considered background.

Thresholding and morphology are the least complex methods used to recover structure. Images are transformed according to some metric that is then thresholded to determine background from foreground. Results can be filtered with mathematical morphology applied both before and after the image is thresholded to account for a limited number of geometric and/or spatial cues.

To our knowledge, relatively little work has been performed for 3D TEE endocardial segmentation: this includes work by Wolf et al. [15] and Kucera et al. [16]. We describe a novel approach to 3D TEE endocardial wall segmentation based on 3D level sets. Foundational work on level set and recent developments can be found in the work by Mumford and Shah, Caselles et al., Malladi and Sethian et al., and Li et al. [21–24]. Our work extends the variational formulation developed by Li et al. [24] and uses a unique energy function specifically designed for the 3D TEE modality. This method, described in Sections 2 and 3, shows promising results, as presented in Section 4.

2 3D Level Sets

We employ a dynamic surface method to find the endocardial boundaries. It exploits a 3D level set approach and works as follows: at time $t = 0$, a dynamic surface is initialized in the atrial and/or intraventricular cavities. This dynamic surface is then obtained at any subsequent time t by considering an evolving function $\phi(x, y, z, t)$. The dynamic surface is found as $S(t)$, the zero level set of $\phi(\cdot)$, i.e., $S(t) = \{(x, y, z)|\phi(x, y, z, t) = 0\}$. $\phi(\cdot)$ evolves under a driving force which is designed to expand the surface until it reaches the intensity boundaries marking the inner walls of the atrial and ventricular cavities. An inhibition function $g(\cdot)$, detailed later, stops the dynamic surface when it meets these walls boundaries. Following [24], our time evolution equation is expressed as

$$\frac{\partial \phi}{\partial t} = -\frac{\delta E}{\delta \phi}, \tag{1}$$

where the right hand side of (1) denotes the Gâteaux derivative.

The energy $E(\phi)$ includes three terms and is defined as

$$E(\phi) = \mu P(\phi) + \lambda A_g(\phi) + \nu V_g(\phi). \tag{2}$$

As in [24], our specification of the evolution equation of $\phi(\cdot)$ includes a weight μ and penalty term $P(\phi)$ to evolve ϕ so that, at all times, it closely approximates a signed distance function. This feature obviates the need for re-initialization and keeps the surface well-behaved. This penalty is expressed as

$$P(\phi) = \int_\Omega \frac{1}{2}(|\nabla \phi| - 1)^2 dx\, dy\, dz, \tag{3}$$

where $\nabla \phi$ is the gradient of ϕ and $\Omega \subset R^3$ is the domain of ϕ.

The second and third terms $A_g(\phi)$ and $V_g(\phi)$ in (2) correspond to the surface area and volume, and drive the surface's evolution to the desired goals. By balancing weights λ and ν, we can maintain regularity as the surface expands by limiting surface area growth and forcing volume expansion. The weight ν is chosen here to be negative so that the surface expands. The terms $A_g(\phi)$ and $V_g(\phi)$ are expressed as

$$A_g(\phi) = \int_\Omega g\delta(\phi)\, |\nabla \phi|\ dx\, dy\, dz, \tag{4}$$

and

$$V_g(\phi) = \int_\Omega gH(-\phi)\ dx\,dy\,dz, \tag{5}$$

where $\delta(\phi)$ denotes the Dirac delta function, and $H(\phi)$ is the Heaviside function.

Equations (4) and (5) contain an inhibition function $g(\cdot)$, mentioned earlier, that is designed to abate the motion of the dynamic boundary in places corresponding to the myocardium and mitral valve leaflets location. This function is detailed in the next section.

After reforming the terms from (2), (4), and (5) into (1), and using the Gâteaux derivative, the evolution of ϕ can be expressed as

$$\frac{\partial \phi}{\partial t} = \mu \left[\Delta\phi - \nabla\cdot\left(\frac{\nabla\phi}{|\nabla\phi|}\right)\right] + \lambda\delta(\phi)\,\nabla\cdot\left(g\frac{\nabla\phi}{|\nabla\phi|}\right) + \nu g\delta\left(\phi\right), \tag{6}$$

where $\nabla\cdot$ denotes the divergence and Δ the Laplacian operators. This equation specifies a time-update evolution equation for $\partial\phi/\partial t$, which corresponds to a form of steepest descent. This equation is discretized to evolve the function ϕ, thus minimizing the objective functional $E(\phi)$.

To close this section we detail the derivation of (6) . To this end we wish to find the first variation of the energy functional

$$E(\phi) = \int_\Omega \left[\frac{\mu}{2}\left(|\nabla\phi|-1\right)^2 + \lambda g\delta(\phi)|\nabla\phi| + \nu g H(-\phi)\right] dV. \tag{7}$$

For future use, we note that $H(-\phi) = 1 - H(\phi)$ and that $H'(\phi) = \delta(\phi)$. Let ϕ be the minimizing function of E, ψ be any other function, and τ be a scalar, then we have

$$\frac{d}{d\tau}E(\phi + \tau\psi)\bigg|_{\tau=0} = 0. \tag{8}$$

The derivatives of the three terms in (7) are given by

$$\frac{d}{d\tau}E_1(\phi + \tau\psi) = \mu\int_\Omega \left(|\nabla\phi + \tau\nabla\psi|-1\right)\frac{\nabla\phi + \tau\nabla\psi}{|\nabla\phi + \tau\nabla\psi|}\cdot\nabla\psi\, dV, \tag{9}$$

$$\begin{aligned}\frac{d}{d\tau}E_2(\phi + \tau\psi) = \lambda\int_\Omega \Bigg[& g\delta(\phi + \tau\psi)\frac{\nabla\phi + \tau\nabla\psi}{|\nabla\phi + \tau\nabla\psi|}\cdot\nabla\psi \\ &+ g\delta'(\phi + \tau\psi)\,|\nabla\phi + \tau\nabla\psi|\,\psi\Bigg] dV,\end{aligned} \tag{10}$$

and

$$\frac{d}{d\tau}E_3(\phi + \tau\psi) = -\nu\int_\Omega g\delta(\phi + \tau\psi)\psi\, dV. \tag{11}$$

Evaluated at $\tau = 0$ these become

$$\frac{d}{d\tau}E_1(\phi + \tau\psi)\bigg|_{\tau=0} = \mu\int_\Omega \left(|\nabla\phi|-1\right)\frac{\nabla\phi}{|\nabla\phi|}\cdot\nabla\psi\, dV, \tag{12}$$

$$\frac{d}{d\tau}E_2(\phi+\tau\psi)\bigg|_{\tau=0} = \lambda\int_\Omega \left[g\delta(\phi)\frac{\nabla\phi}{|\nabla\phi|}\cdot\nabla\psi + g\delta'(\phi)|\nabla\phi|\psi\right]dV, \quad (13)$$

and

$$\frac{d}{d\tau}E_3(\phi+\tau\psi)\bigg|_{\tau=0} = -\nu\int_\Omega g\delta(\phi)\psi\,dV. \quad (14)$$

Using Green's first identity,

$$\int_\Omega \psi\Delta\phi + \nabla\phi\cdot\nabla\psi\,dV = \int_{\partial\Omega}\psi\nabla\phi\cdot d\boldsymbol{a}, \quad (15)$$

(12) may be recast as

$$\begin{aligned}\mu\int_\Omega (|\nabla\phi|-1)\frac{\nabla\phi}{|\nabla\phi|}\cdot\nabla\psi\,dV &= -\mu\int_\Omega \nabla\cdot\left(\nabla\phi-\frac{\nabla\phi}{|\nabla\phi|}\right)\psi\,dV \\ &= -\mu\int_\Omega\left[\Delta\phi-\nabla\cdot\left(\frac{\nabla\phi}{|\nabla\phi|}\right)\right]\psi\,dV, \quad (16)\end{aligned}$$

where the surface term in (15) has been omitted based on the assumption that the variation is zero on the boundary (i.e., the boundary values of the functions over which E is considered are specified and hence $\psi = 0$ on $\partial\Omega$). Similarly, the first term in (13) becomes

$$\lambda\int_\Omega g\delta(\phi)\frac{\nabla\phi}{|\nabla\phi|}\cdot\nabla\psi\,dV = -\lambda\int_\Omega\left[g\delta'(\phi)|\nabla\phi|+\delta(\phi)\nabla\cdot\left(g\frac{\nabla\phi}{|\nabla\phi|}\right)\right]\psi\,dV. \quad (17)$$

Since, from (8), we have $\frac{d}{d\tau}E(\phi+\tau\psi)\big|_{\tau=0} = 0$, then

$$\int_\Omega\left\{-\mu\left[\Delta\phi-\nabla\cdot\left(\frac{\nabla\phi}{|\nabla\phi|}\right)\right]-\lambda\delta(\phi)\nabla\cdot\left(g\frac{\nabla\phi}{|\nabla\phi|}\right)-\nu g\delta(\phi)\right\}\psi\,dV = 0. \quad (18)$$

As this must be true for any ψ, the portion of the integrand in braces must be identically zero for the minimizer ϕ. We therefore define the Gâteaux derivative

$$\frac{\partial E}{\partial\phi} = -\mu\left[\Delta\phi-\nabla\cdot\left(\frac{\nabla\phi}{|\nabla\phi|}\right)\right]-\lambda\delta(\phi)\nabla\cdot\left(g\frac{\nabla\phi}{|\nabla\phi|}\right)-\nu g\delta(\phi), \quad (19)$$

such that the minimizer ϕ satisfies the Euler-Lagrange equation $\frac{\partial E}{\partial\phi} = 0$.

3 Inhibition Function

Our design for the inhibition function $g(\cdot)$ takes into account three components: the output of a k-means clustering, the output of a thin tissue detector using a structure tensor, and the TEE intensity gradient.

k-means clustering provides a good outline of the endocardium and surrounding structure. It is obtained after low pass filtering and intensity remapping to address any signal drop-off far from the TEE frustum apex (corresponding to

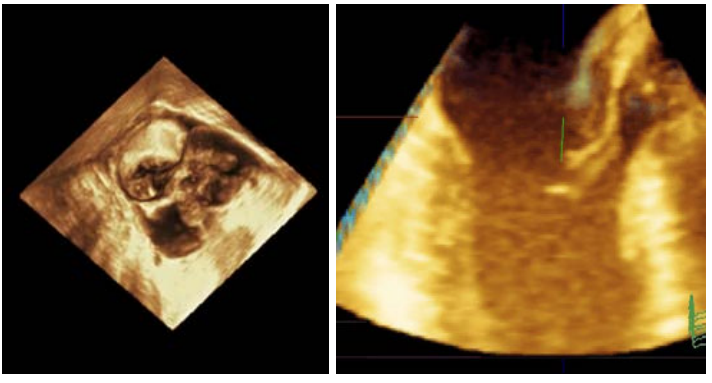

(a) (b)

Fig. 1. 3D TEE: (a) top view from the left atrium showing the mitral valve, the aortic valve, and the left ventricle; (b) side view showing the left atrium, the mitral valve leaflets, the aortic valve and the left ventricle

the TEE probe location). We denote the output of the k-means algorithm by the indicator function $J_{KM}(x, y, z)$, equal to one where the k-means algorithm clustered the darker voxels (including the intraventricular and intra-atrial cavities), and zero otherwise (including the myocardial areas).

Additional information on the heart wall and anatomical structures such as the trabeculae carneae and chordae tendineae is indicated by a variation in intensity in the 3D TEE which is captured by the function $ed(\cdot)$, as in:

$$ed(x, y, z) = \frac{1}{1 + a|\nabla G * I(x, y, z)|^2}. \tag{20}$$

where $\nabla G * I$ is the gradient of the Gaussian-smoothed TEE intensity. This function represents a 'negative' of the gradient magnitude map, taking small values for high gradient magnitudes, and values close to 1 for small gradient magnitudes. This gradient-based definition of $ed(\cdot)$ might be an issue for echocardiography images with limited contrast. We have found however that it works adequately with TEE imaging, which allows a close "view" into the left heart complex and exhibits good contrast when compared to other cardiac ultrasound imaging techniques such as transthoracic echocardiography.

The third term in our specification of the inhibition function exploits the structure tensor to detect the location of thin tissue such as the mitral or aortic valve leaflets, whose detection may be sometimes problematic using the two former methods.

Given a volume of intensity values $f(\mathbf{x})$ where $\mathbf{x}$ is the (x, y, z) coordinate of the voxel, one can approximate the values surrounding a point in the volume $\mathbf{x}_0$ in a second-order Taylor series fashion as

$$f(\mathbf{x}) \approx f(\mathbf{x}_0) + (\mathbf{x} - \mathbf{x}_0)^T \nabla f_0 + \frac{1}{2}(\mathbf{x} - \mathbf{x}_0)^T \nabla^2 f_0 (\mathbf{x} - \mathbf{x}_0), \tag{21}$$

where ∇f_0 and $\nabla^2 f_0$ denote the gradient vector and the Hessian matrix at $\mathbf{x}_0$ respectively. From this approximation, it is important to note that the varying intensities surrounding $\mathbf{x}_0$ is spanned by the eigenvectors of the Hessian matrix. The eigenvalues corresponding to these eigenvectors can be used to define a new space that is invariant under orthonormal transformations. Tissue classification can be performed in this space. From [25, 26], thin planar structures can be found as follows: Let $\mathbf{e}_1(\mathbf{x})$, $\mathbf{e}_2(\mathbf{x})$, and $\mathbf{e}_3(\mathbf{x})$ be the eigenvectors of the Hessian matrix $\nabla^2 f$ where $\mathbf{e}_1(\mathbf{x})$ corresponds to the eigenvector with the largest eigenvalue $\lambda_1(\mathbf{x})$, $\mathbf{e}_2(\mathbf{x})$ corresponds to the eigenvector with the next largest eigenvalue $\lambda_2(\mathbf{x})$, and $\mathbf{e}_3(\mathbf{x})$ corresponds to the eigenvector with the smallest eigenvalue $\lambda_3(\mathbf{x})$ (i.e., $\lambda_1 \geq \lambda_2 \geq \lambda_3$). A measure of the planarity of the surrounding local structure can be defined by:

$$S_{sheet}\{f\} = \begin{cases} |\lambda_3| \cdot w(\lambda_2, \lambda_3) \cdot w(\lambda_1, \lambda_3), \lambda_3 < 0, \\ 0 \qquad\qquad\qquad\qquad\qquad \text{otherwise.} \end{cases} \tag{22}$$

where $w(\lambda_s, \lambda_t)$ is defined by:

$$w(\lambda_s, \lambda_t) = \begin{cases} \left(1 + \frac{\lambda_s}{|\lambda_t|}\right)^{\gamma}, & \lambda_t \leq \lambda_s < 0, \\ \left(1 - \alpha\frac{\lambda_s}{|\lambda_t|}\right)^{\gamma}, & \frac{|\lambda_t|}{\alpha} > \lambda_s > 0, \\ 0 & \text{otherwise.} \end{cases} \tag{23}$$

γ controls the sharpness of selectivity and α controls the asymmetrical characteristic in the negative and positive regions of λ_s, with $0 < \alpha \leq 1$. We found that $\gamma = 0.5$ and $\alpha = 0.25$ work well in our experiments. We denote by $J_l(x, y, z)$ the inverse of the indicator function denoting the leaflet position found by the structure tensor method.

Collecting the various terms together, our final specification for the level set inhibition function is given by:

$$g(x, y, z) = J_{KM}(x, y, z) \cdot J_l(x, y, z) \cdot ed(x, y, z). \tag{24}$$

4 Experiments

Intraoperative real-time 3D TEE full volume sequences of the left heart were collected from patients undergoing surgery. 3D TEE acquisition was performed using an iE33 Philips console with a Philips X2-T Live 4D TEE probe (Philips Medical Systems, Bothell, WA). The TEE cube sizes were 208×208×224. The 3D TEE probe was operated at frequencies ranging from 3 to 5 MHz. The pixels spatial resolutions were respectively 0.666×0.657×0.580 mm or approximately 1.10 mm diagonal voxel resolution. A 7 breath-hold cycle acquisition protocol was employed leading to a frame rate of close to 50 Hz.

In our experiments, we found the following parameters values to work well for left ventricle and atrium segmentation: $\lambda = 4$, $\mu = 0.04$, $\nu = -6$, and $a = 300$. The parameter values were kept unchanged for all the experiments as we benchmarked the segmentation method. Benchmarking was performed using four 3D

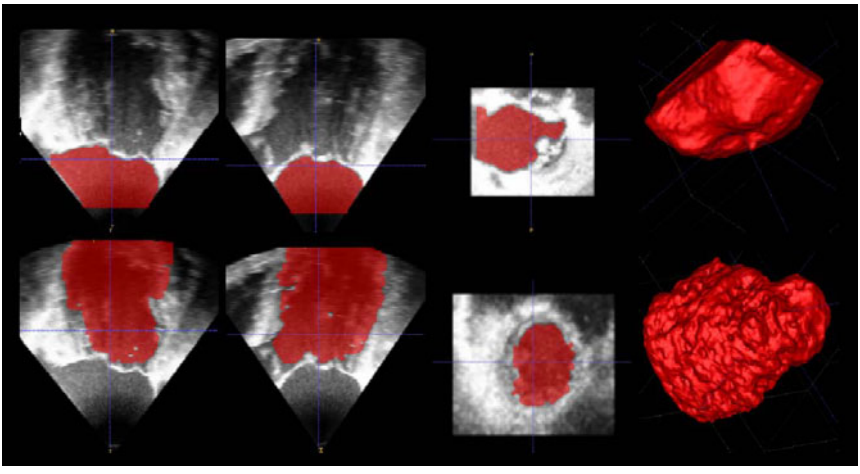

Fig. 2. Intra-atrial cavity (top) and intraventricular cavity (bottom) segmentation. In each row, from left to right: long axis/two chamber, long axis/four chambers, short axis, and 3D rendered views.

TEE datacubes. Ground truth segmentation of the intra-atrial and intraventricular cavities was done by experts on full volumes, using hand segmentation on all short axis, long axis/two chamber, and long axis/four chamber views. In all, this involved hand segmentation of 2560 view planes to allow the computation of errors and DICE numbers. We found a mean absolute error $m = 2.29$ mm with associated standard deviation $\sigma = 2.70$ mm, a root mean square error of $r = 3.56$ mm, and a DICE number of $d = 85.60\%$. Examples of 3D TEE cubes are shown in Fig. 1. Examples of the resulting segmentation of full TEE cubes are shown in Fig. 2.

5 Conclusions

We describe a novel 3D segmentation method to detect endocardial walls from 3D TEE. Promising results are found using intraoperative TEE data. Challenging factors still remain, including the detection of the walls and the characterization of performance in areas with strong trabeculation, such as close to the ventricular apex, where we also found sizable inter-expert ground truth segmentation variation. Future goals are to address these challenges and limitations.

Acknowledgments

We wish to thank Profs. D. Yuh (JHMI/Cardiothoracic Surgery) and E. McVeigh (JHU BME) for providing data and useful discussions. This project was supported by JHU APL Science and Technology Research and Development funds and NIH NHLBI R21HL098765. The content is solely the responsibility of the authors and does not necessarily represent the official views of the National Heart, Lung, And Blood Institute or the National Institutes of Health.

References

1. Burlina, P., Sprouse, C., DeMenthon, D., Jorstad, A., Juang, R., Contijoch, F., Abraham, T., Yuh, D., McVeigh, E.: Patient-specific modeling and analysis of the mitral valve using 3D-TEE. In: Information Processing in Computer-Assisted Interventions, pp. 135–146 (2010)
2. Sprouse, C., Yuh, D., Abraham, T., Burlina, P.: Computational hemodynamic modeling based on transesophageal echocardiographic imaging. In: Proc. Int. Conf. Engineering in Medicine and Biology Society, vol. 2009, pp. 3649–3652 (2009)
3. Mukherjee, R., Sprouse, C., Abraham, T., Hoffmann, B., McVeigh, E., Yuh, D., Burlina, P.: Myocardial motion computation in 4D ultrasound. In: Proc. Int. Symp. on Biomedical Imaging (2011)
4. Noble, J., Boukerroui, D.: Ultrasound image segmentation: A survey. IEEE Transactions on Medical Imaging 25(8), 987–1010 (2006)
5. Noble, J.: Ultrasound image segmentation and tissue characterization. Proc. of the Institution of Mechanical Engineers, Part H: Journal of Engineering in Medicine 224(2), 307–316 (2010)
6. Hammoude, A.: Endocardial border identification in two-dimensional echocardiographic images: review of methods. Computerized Medical Imaging and Graphics 22(3), 181–193 (1998)
7. Mitchell, S., Lelieveldt, B., van der Geest, R., Bosch, H., Reiber, J., Sonka, M.: Multistage hybrid active appearance model matching: segmentation of left and right ventricles in cardiac MR images. IEEE Transactions on Medical Imaging 20, 415–423 (2001)
8. O'Brien, S., Ghita, O., Whelan, P.: Segmenting the left ventricle in 3D using a coupled ASM and a learned non-rigid spatial model. The MIDAS Journal 49 (August 2009)
9. Wijnhout, J., Hendriksen, D., Assen, H.V., der Geest, R.V.: LV challenge LKEB contribution: Fully automated myocardial contour detection. The MIDAS Journal 43 (August 2009)
10. Angelini, E., Homma, S., Pearson, G., Holmes, J., Laine, A.: Segmentation of real-time three-dimensional ultrasound for quantification of ventricular function: a clinical study on right and left ventricles. Ultrasound in Medicine & Biology 31(9), 1143–1158 (2005)
11. Duan, Q., Angelini, E., Laine, A.: Real-time segmentation by Active Geometric Functions. Computer Methods and Programs in Biomedicine 98(3), 223–230 (2010)
12. Qu, Y., Chen, Q., Heng, P., Wong, T.: Segmentation of left ventricle via level set method based on enriched speed term. In: Barillot, C., Haynor, D.R., Hellier, P. (eds.) MICCAI 2004. LNCS, vol. 3216, pp. 435–442. Springer, Heidelberg (2004)
13. Chen, Y., Tagare, H., Thiruvenkadam, S., Huang, F., Wilson, D., Gopinath, K., Briggs, R., Geiser, E.: Using prior shapes in geometric active contours in a variational framework. International Journal of Computer Vision 50(3), 315–328 (2002)
14. Han, C., Lin, K., Wee, W., Mintz, R., Porembka, D.: Knowledge-based image analysis for automated boundary extraction of transesophageal echocardiographic left-ventricular images.. IEEE Transactions on Medical Imaging 10(4), 602 (1991)
15. Wolf, I., Hastenteufel, M., De Simone, R., Vetter, M., Glombitza, G., Mottl-Link, S., Vahl, C., Meinzer, H.: ROPES: A semiautomated segmentation method for accelerated analysis of three-dimensional echocardiographic data. IEEE Transactions on Medical Imaging 21(9), 1091–1104 (2003)

16. Kucera, D., Martin, R.: Segmentation of sequences of echocardiographic images using a simplified 3D active contour model with region-based external forces. Computerized Medical Imaging and Graphics 21(1), 1–21 (1997)
17. Cousty, J., Najman, L., Couprie, M., Clment-Guinaudeau, S., Goissen, T., Garot, J.: Segmentation of 4D cardiac MRI: automated method based on spatio-temporal watershed cuts. Image and Vision Computing 28(8), 1229–1243 (2010)
18. Ben Ayed, I., Punithakumar, K., Li, S., Islam, A., Chong, J.: Left ventricle segmentation via graph cut distribution matching. In: Yang, G.-Z., Hawkes, D., Rueckert, D., Noble, A., Taylor, C. (eds.) MICCAI 2009. LNCS, vol. 5762, pp. 901–909. Springer, Heidelberg (2009)
19. Lu, Y., Radau, P., Connelly, K., Dick, A., Wright, G.: Automatic image-driven segmentation of left ventricle in cardiac cine MRI. The MIDAS Journal 49 (August 2009)
20. Lempitsky, V., Verhoek, M., Noble, J.A., Blake, A.: Random forest classification for automatic delineation of myocardium in real-time 3D echocardiography. In: Ayache, N., Delingette, H., Sermesant, M. (eds.) FIMH 2009. LNCS, vol. 5528, pp. 447–456. Springer, Heidelberg (2009)
21. Mumford, D., Shah, J.: Optimal approximations by piecewise smooth functions and associated variational problems. Communications on Pure and Applied Mathematics 42(5), 577–685 (1989)
22. Malladi, R., Sethian, J., Vemuri, B.: Shape modeling with front propagation: A level set approach. IEEE Transactions on Pattern Analysis and Machine Intelligence 17(2), 158–175 (2002)
23. Caselles, V., Kimmel, R., Sapiro, G.: Geodesic active contours. International Journal of Computer Vision 22(1), 61–79 (1997)
24. Li, C., Xu, C., Gui, C., Fox, M.D.: Level set evolution without re-initialization: a new variational formulation. In: Proc. IEEE Computer Society Conf. on Computer Vision and Pattern Recognition, pp. 430–436. IEEE Computer Society, Los Alamitos (2005)
25. Sato, Y., Westin, C., Bhalerao, A., Nakajima, S., Shiraga, N., Tamura, S.: Tissue classification based on 3d local intensity structures for volume rendering. IEEE Transactions on Visualization and Computer Graphics (6) (2000)
26. Huang, A., Nielson, G., Razdan, A., Farin, G., Baluch, D., Capco, D.: Thin structure segmentation and visualization in three-dimensional biomedical images: a shape-based approach. IEEE Transactions on Visualization and Computer Graphics 12(1), 93–102 (2006)